

## X-ray analysis of changes to the atomic structure around Ni associated with the interdiffusion and mechanical alloying of pure Ni and Mo powders

G. Cocco

*Department of Chemistry, University of Sassari, 07100 Sassari, Italy*

S. Enzo

*Department of Chemical Physics, University of Venice, 30123 Venice, Italy*

N. T. Barrett

*Département de Physique Générale, Centre d'Etudes Nucléaires de Saclay, 91911 Gif-sur-Yvette, France  
and Laboratoire pour l'Utilisation du Rayonnement Electromagnétique, Batiment 209D, Centre Universitaire Paris-Sud,  
91405 CEDEX, France*

K. J. Roberts

*Department of Pure and Applied Chemistry, University of Strathclyde, Glasgow, G1 1XL, United Kingdom  
and SERC Daresbury Laboratory, Warrington WA4 4AD, United Kingdom*

(Received 19 February 1991; revised manuscript received 12 November 1991)

We have applied a combination of x-ray diffraction and x-ray-absorption spectroscopy to probe, in a self-consistent way, the bulk and local structural changes, respectively, associated with the mechanical alloying of pure metallic powders of Ni and Mo. From a careful analysis using an analytical atomic-subshell, we show that the Ni (fcc) atoms are totally involved in the alloying reaction with Mo (bcc) atoms taking up substitutional positions in the Ni (fcc) lattice. Prior to the formation of the amorphous phase, at milling times  $\approx 10$  h, an intermediate and highly distorted NiMo phase forms with an internal strain of  $\approx 2.1 \times 10^{-3}$ . The release of this strain with milling time corresponds to an increase in the Mo content in the alloy and the nucleation of an amorphous phase together with a subsequent loss of long-range order of the Ni lattice. The resultant amorphous phase closely resembles  $\delta$ -NiMo and after milling times  $\approx 54$  h has a nominal composition of Ni<sub>50</sub>Mo<sub>38</sub>. Its formation is associated with Mo in a residual but distorted bcc environment characterized by a particle size of  $\approx 70$  nm and an internal strain of  $1.8 \times 10^{-3}$ . The detailed local structure around Ni atoms during this process is presented and discussed.

### I. INTRODUCTION

Milling is commonly used in the processing of industrial powders both to define a particular parameter, such as size, shape, and structure, as well as to facilitate the intimate interaction of the components of mixed systems for subsequent matrix consolidation. Milling techniques have also provided an effective part of the preparation of high-temperature alloys.<sup>1,2</sup> In spite of such technological applications, the fundamental and mechanistic basis for the physical and chemical processes actually occurring during milling is poorly understood and defined. In contrast the more recent interest in amorphous metallic phases produced by the cold rolling of metal foils and by mechanical alloying have stimulated a considerable interest in the fundamental aspects associated with solid-state reactions. A distinction of terminology between mechanical alloying (MA), for a starting mixture of pure elements, and mechanical grinding, for intermetallic compounds, is generally made.

Since the work of Koch *et al.*,<sup>3</sup> a wide range of alloys has been found to "amorphize" using solid-state amorphization (SSA) reactions.<sup>4</sup> However, much of the work has been carried over from the technological environment of ball milling and there is a clear need to examine the MA

of crystalline materials to establish unequivocally which kind of materials are "truly" amorphous rather than micro- or nanocrystalline. In many cases the simultaneous observation of both crystalline and amorphous phases after MA and the "heterogeneous" nature of the resultant product can lead to much confusion in elucidating and defining SSA processes which are not, as yet, established on any firm quantitative basis.

Schematically, two main mechanisms have been envisaged for attaining an amorphous state by SSA.

(i) The first assumes that fragmentation of crystallite size and the introduction of a high level of lattice defects are responsible for SSA. This model is supported by a study<sup>5</sup> of amorphization by mechanical grinding which showed the possibility of amorphizing Co-Y intermetallics by the continuous fragmentation and disordering processes associated with a prolonged milling action. If this simple mechanism holds, it should be possible to amorphize also pure elements.

(ii) In the second mechanism the responsibility for SSA transformations to an amorphous state have been attributed to a fast diffusion of one element into the host matrix of the other. The driving force for such diffusion is derived from the strong negative heat of mixing. If this mechanism occurs, we should be able<sup>6</sup> to observe

amorphization at relatively low MA times and eventually follow the insertion of one element into the host matrix as suggested by Dubois.<sup>7</sup>

SSA by MA can also be assisted by moderate thermal treatment at a temperature below the crystallization temperature of compounds. Such a process has been observed in the case of artificial multilayered binary metal systems.<sup>8</sup> Fast diffusion is generally favored by putting fresh surfaces of pure elements into contact and this is expected to produce an amorphous phase after reaching a certain degree of intimate mixing between the two metals. As this latter requirement can also be achieved through the reduction of the average crystallite size the difference in these two mechanisms is, to a certain extent, one of terminology.

The evaluation of the structural aspects associated with the nucleation and development of the amorphous phase by MA is thus crucial for our understanding and definition of SSA processes. The detailed structural characterization of these processes requires structural probes capable of examining changes to both the long- and short-range atomic correlations associated with MA. This requirement can be met by the application of the complementary techniques of x-ray diffraction (XRD) and extended x-ray-absorption fine structure (EXAFS) as XRD gives information on long-range order, crystal structure, crystal size, lattice strain, and amorphous content while EXAFS gives detailed information on short-range order and the shape of the radial distribution function (RDF) around the alloying elements.

This paper presents a self-consistent application of this combination of XRD and EXAFS to probe the detailed structural changes that take place in the atomic environment around Ni during the MA of pure elemental powders of Ni and Mo. Our aim has been to understand the structural path through which the elemental powders are driven before achieving amorphization in order to probe the nature of the atomic forces responsible for the MA process.

## II. EXPERIMENTAL

### A. Sample preparation

Pure crystalline elemental powders of Ni and Mo (Alfa Products, purity better than 99.99%) were mixed in equiatomic ratio in a hardened tool steel vial with a ball to powder weight ratio 10:1 and milled with a SPEX mixer and mill, model 8000. The milling was performed at room temperature and under argon atmosphere in a dry box, and care was taken to keep the oxygen contamination lower than 10 ppm. The progress of amorphization by milling was examined by periodically withdrawing small quantities of the powder for examination using XRD and EXAFS.

### B. XRD data collection

XRD powder spectra (Cu  $K\alpha$  radiation) of the pure elemental powders, the milled mixtures, and of an  $\alpha\text{SiO}_2$  well-crystallized reference standard were collected with a Philips vertical goniometer with x rays from a highly sta-

bilized 1.5-kW generator. The diffracted rays were monochromated with a focusing graphite crystal and detected with a scintillation counter. XRD data were collected over an angular range of  $2\theta$  from  $20^\circ$  to  $145^\circ$  corresponding to a wave-vector range of  $14\text{--}75\text{ nm}^{-1}$ . The scans were collected in the step-count preset-time mode until a satisfactory signal-to-noise ratio was reached.

### C. EXAFS data collection

The EXAFS data were collected at the synchrotron-radiation source (SRS) at Daresbury Laboratory. The SRS operated in a dedicated mode at an energy of 2 GeV with a stored beam current typically of  $\approx 150\text{ mA}$  and a lifetime of  $\approx 12\text{ h}$ . Spectra were taken above the  $K$  edges of Ni (8.33 keV) and Mo (20.00 keV) using stations 7.1 and 9.2, and silicon (111) and (220), double crystal monochromators, respectively. The latter were detuned to provide harmonic rejection.<sup>9</sup> This set up provides an energy band pass of  $\approx 10^{-4}$  which at the Ni  $K$  edge gives an energy resolution of  $\approx 0.5\text{ eV}$ . The incident and transmitted intensities were measured by ionization chambers, and care was taken to keep the statistical error below 0.1%. Energy calibration was carried out using Ni and Mo foils with the aid of a third ion chamber. The samples were prepared to thicknesses such that the product of the absorption coefficient and the sample thickness was  $\approx 2$ . The principle risk of sample contamination came from the steel balls used in milling; however, absorption measurements revealed no traces of these elements.

## III. DATA ANALYSIS

### A. XRD data

#### 1. Peak profile fitting

For the assessment of structural changes from line-profile analysis it is usual to analyze data normalized with respect to the diffraction wavelength, i.e., we display the data as a function of the scattering wave vector  $S_{hkl}$ , where

$$S_{hkl} = 4\pi/\lambda \sin\theta \quad (1)$$

and the symbols have their usual meaning. The instrument function for the XRD data was determined with the aid of an  $\alpha\text{-SiO}_2$  reference standard over the angular range of the diffractometer. The instrumental function was convoluted with a broadening function and the resulting shape adjusted to fit the experimental data by the use of an improved profile-fitting procedure. For the adjustable broadening function we used a pseudo-Voigt function, i.e., a linear combination of Lorentz and Gauss functions

$$pV(x) = I_p \{ n(1+x^2)^{-1} + (1-n) \exp[-x^2(\ln 2)] \} , \quad (2)$$

where

$$x = (2\theta - 2\theta_0)/w_1 A . \quad (3)$$

The adjustable parameters for each peak are  $I_p$ , intensity at the peak maximum;  $2\theta_0$  is the location of the peak maximum;  $w_1$  is the peak width at half maximum on the left-hand side;  $A$  is the peak symmetry which equals the ratio  $w_1/w_r$ ; and  $n$  is the mixing factor between 0 (Gauss peak) and 1 (Lorentz peak). The entire procedure of data collection and treatment for deconvolution has been reported earlier.<sup>10–12</sup>

### 2. Estimation of amorphous-phase composition

The formation of an amorphous phase can be detected by XRD through the observation of a broad “halo” in the diffraction pattern at a wave vector commensurate with average atomic correlations in the material. We can estimate the composition by comparing the ratio ( $R$ ) of the relative areas of the halo to one of the main Bragg diffraction peaks from

$$x = y[(1-R)/(1+R)], \quad (4)$$

where  $x$  and  $y$  are the atomic fractions of the two components in the amorphous alloy. For  $\text{Ni}_{50}\text{Mo}_{50}$  this simple relation can be used to give a reasonable estimate (> 10%) of the composition due to the closeness in electron density for Ni (fcc), Mo (bcc), and  $\delta$ -NiMo which are 2560, 2700, and 2650  $\text{nm}^{-3}$ , respectively.

### 3. Estimation of particle size and strain

Two separate particle size and strain effects the diffraction line profile were analyzed using both the simplified method<sup>13</sup> and Warren-Averbach (WA) Fourier method.<sup>14</sup> Particle strain is dependent on the wave vector  $S$  whereas particle size is not.

The simplified method is a variant of the Williamson and Hall (WH) approach<sup>15</sup> in which the integral breadth ( $\Delta S$ ) of the diffraction peak is plotted as a function of  $S_{hkl}^2$ . The integral width is calculated, after peak fitting and allowing for the instrumental broadening function, from

$$\Delta S_{hkl} = \{[\pi/\ln(2)]^{1/2}n + (1-n)\pi\} W_1(1+A)/2. \quad (5)$$

In the Fourier WA method the Fourier transforms of the multiple-order peak profiles are plotted as a function of  $S_{hkl}^2$ .

The two methods differ in that the validity of the simplified WH approach relies on the absence of preferred orientation, which seems reasonable for MA metallic powders. Additionally in the WH approach only average figures of strain and connected size are obtained, whereas using the Fourier WA method it is possible to account for distributions in both size and strain.

## B. EXAFS data

### 1. Data-reduction and curve-fitting procedures

EXAFS data were calibrated and background subtracted using the standard programs available at Daresbury Laboratory and analyzed using the least-squares curved-wave program *EXCURV88*.<sup>16</sup> *EXCURV88* employs a

curved-wave formalism, particularly adapted to solving amorphous or disordered structures. The normalized EXAFS function  $[\chi(E)]$  is given by

$$\chi(E) = (\mu - \mu_0)/\mu_0, \quad (6)$$

where  $\mu$  is the absorption coefficient and  $\mu_0$  is the smooth background term. The generally accepted formalism for EXAFS for a given central atom treats it as a simple sum of sinusoidal waves  $[\chi(k)]$ , each arising from a near-neighbor shell within the structure. In the plane-wave approximation, we have

$$\chi(k) = - \sum_i \left[ \left[ \frac{N_i}{kr_i^2} \right] F_i(k) S_0^2(k) \exp \left[ \frac{-r_i}{\Gamma(k)} \right] \right. \\ \left. \times \exp(-2k^2\sigma^2) \sin[2kr_i + \phi_i(i)] \right], \quad (7)$$

where  $r_i$  is the distance from the absorbing atom to shell  $i$ ;  $\phi_i(k)$  is the total phase shift experienced by the photoelectron;  $F_i(i)$  is the backscattering amplitude of the neighboring atoms;  $N_i$  is the coordination number of the  $i$ th shell;  $S_0^2(k)$  and  $\exp[-r_i/\Gamma(k)]$  are damping terms corresponding, respectively, to multielectron processes within the central atom and the effective mean free path of the photoelectron in the material; and  $\exp(-2k^2\sigma^2)$  is a “Debye-Waller” type term. In the latter expression  $\sigma^2$  describes structural and thermal disorder and represents the mean-square average of the difference in atomic displacements. The photoelectron wave number  $k$  is given by

$$k = [(2m/h^2)(E - E_{\text{edge}} + E_0)]^{1/2}, \quad (8)$$

where  $E_{\text{edge}}$  is the energy position of the absorption-edge threshold and  $E_0$  (typically  $\approx 10$ – $20$  eV) is an energy offset which represents the difference between the mean potential energy of the solid and that of the lowest unoccupied energy level in the conduction band.  $E_0$  was defined as the energy at half the maximum step, corrected for the presence of a white line. The pre-edge background, determined by a polynomial interpolation, was subtracted to the whole spectrum. The atomlike smooth contribution  $[\mu_0(E)]$  to the post-edge absorption was reproduced by spline polynomial functions.

One of the problems associated with using EXAFS to analyze the formation of an intermetallic compound such as the Ni-Mo system is that there are no obvious crystal-line reference compounds to determine the atomic backscattering phase shifts and amplitudes.<sup>17</sup> In this study we calculated the backscattering phases for both Ni and Mo using the MUF POT program.<sup>18</sup> MUF POT uses Herman-Skillman wave functions starting from a muffin-tin potential assuming a relaxed 1s core-hole model for the absorbing atom. The resultant phases have been tested against Ni and Mo pure metal spectra with the only parameters varied to fit the reference spectra being  $E_0$ ,  $S_0(k)$ , and  $\Gamma(k)$ . We did *not* refine the phases and assume the values of these parameters to hold for the  $\text{Ni}_{50}\text{Mo}_{50}$  system after

milling. Our approach contrasts to that adopted by Teo *et al.*<sup>17</sup> who fitted different phases, and hence different  $E_0$  values to each of the pair correlations but is, we feel, much more self-consistent in that only one  $E_0$  value is used. The success with which these phases fit the reference spectra by varying only the parameters  $E_0$ ,  $S_0(k)$ , and  $\Gamma(k)$  we feel is due to the more accurate phase calculations using the curved-wave formalism (see Gurman<sup>19</sup>). These refined parameters were transferred and the calculated phase shifts used in the analysis of the data, allowing determination of the structural parameters  $r$ ,  $N$ , and  $\sigma^2$  for each shell of neighbors.

## 2. Allowing for phase cancellation of backscattered phases

We expect to be able to distinguish between Ni and Mo atoms *in the same shell* because of the characteristic forms of the backscattering amplitudes (Teo and Lee<sup>20</sup>). This data, summarized in Fig. 1, illustrate the potential problems associated with phase cancellation in the analysis of the EXAFS data of bimetallic systems such as Ni<sub>50</sub>Mo<sub>50</sub>. This problem has been previously noted by Teo *et al.*<sup>17</sup> and explained, for the analysis of MoFeS<sub>4</sub> cores in double carbanes,<sup>21</sup> that under certain circumstances the Fourier transform (FT) may be drastically attenuated if more than one type of backscatterer is present. The total phase functions  $[\Delta(k)]$  given by

$$\Delta(k) = \{2k(r_1 - r_2) + [\phi_1^{\text{tot}}(k) - \phi_2^{\text{tot}}(k)]\}, \quad (9)$$

where  $r_1, r_2$  and  $\phi_1^{\text{tot}}(k)$ ,  $\phi_2^{\text{tot}}(k)$  are the distances and phase contributions for the two backscattering sites. In particular, if two types of backscatterers are at approximately the same distance, and if the difference in the total phase functions  $[\Delta(i)]$  is close to  $\pi$  over a large part of the  $k$  range, then the amplitude of the FT will be small. Thus any attempt to fit EXAFS without the correct phase shift and nearly the correct distances will result in abnormally small coordination numbers. This will be clearly demonstrated in Sec. IV B in the analysis of the Ni/Mo mixed first shell.

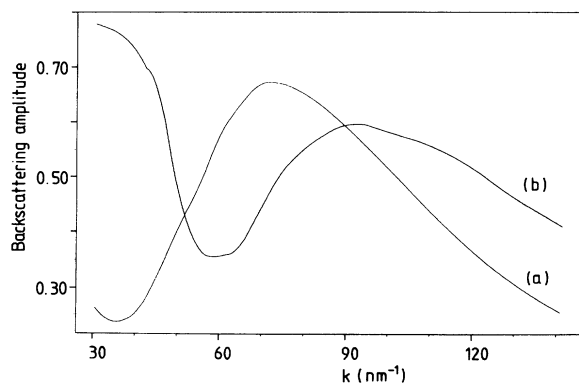


FIG. 1. Wave-vector-dependent backscattering amplitudes calculated from the data of Teo and Lee (Ref. 20) for Ni (a) and Mo (b) showing the effects of phase cancellation as a function of  $k$ .

TABLE I. Radial distribution functions based on the known crystal structure for the Ni ( $a_0=0.3524$  nm) and Mo ( $a_0=0.3147$  nm) starting materials.  $N$  is the coordination number and  $r$  is the shell distance (nm) from the central atom.

Shell	Ni (fcc)		Mo (bcc)	
	$N$	$f$	$N$	$r$
1	12	0.249	8	0.273
2	6	0.353	6	0.315
3	24	0.432	12	0.445

## 3. Subshell analysis

The radial distribution functions (RDF's) for the two starting metals, Ni (fcc) and Mo (bcc), are given in Table I. From this it can be seen that the first shell of Ni is well isolated in terms of distance and thus can be Fourier filtered and analyzed separately. This is not the case for the Mo bcc spectra where we expect in the first coordination shell two subshells located at  $\sqrt{3}/2a_0$  and  $a_0$ , respectively, where  $a_0$ , the Mo bcc lattice parameter, is 0.3154 nm. A further reason for analyzing just the first shell is dictated by the complexity of the system. Because the end stage of the milling process is an amorphous binary alloy, the first shell will very probably contain a distribution of Ni and Mo distances. The complexity of the environment is evident from Fig. 2 which shows a Gaussian-broadened histogram (i.e., broadened with realistic Debye-Waller factors for the temperature) of the partial RDF around Ni in the *crystalline* alloy  $\delta$ NiMo.<sup>22</sup>

Due to the increasing structural disorder expected as a function of milling time we have adopted the subshell method<sup>23</sup> to model the first-shell correlations and hence follow the formation of the amorphous phase as a function of milling time. In this we used the following procedure.

- (i) The data were fitted using 12 subshells each having the fixed coordination number of 1 and allowing only the

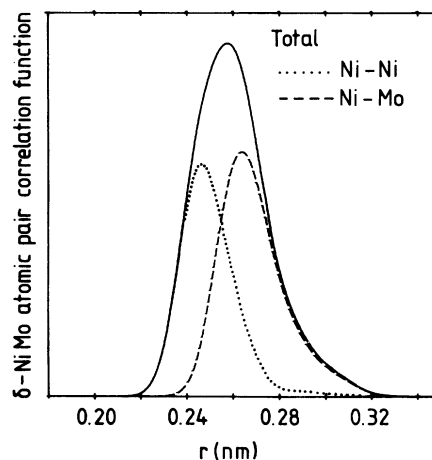


FIG. 2. Atomic pair correlations for  $\delta$ -NiMo showing the atomic distributions for Ni-Ni and Ni-Mo in the first shell of this compound.

atom-atom distances to change, the atom types (either Ni or Mo) being provided from the NiMo phase composition determined by XRD.

(ii) The data were then presented as a partial RDF comprising the 12 shells Gaussian broadened by  $2\sigma^2$  where the Debye-Waller factors are those determined by Teo *et al.*,<sup>17</sup> i.e., 0.000 16 and 0.000 22 nm<sup>2</sup> for Ni-Ni and Ni-Mo, respectively.

Given the total coordination number, and the phase compositions obtainable from XRD data, we are thus able to predict the alloy composition, and therefore the number of Ni and Mo neighbors. We put in the required number of single atom subshells and let the  $r$  values float. The result is a histogram which represents the Ni and Mo partial RDF's around Ni in the amorphous phase.

It should be clear that the use of 12 single-atom subshells does not necessarily mean 12 sets of independent parameters. Examination of the correlation matrix shows strong correlation amongst Ni-Ni and Ni-Mo distances. The use of subshells to establish a possible correlation between neighbors does not make any *a priori* assumptions as to the form of the first-shell radial distribution function. This is not the case if we were to assume, for example, an asymmetric Gaussian distribution. We have preferred to use the subshell method to determine how the Ni and Mo neighbors are grouped together within the first shell. As is shown in Sec. IV B and in Figs. 12–15, the final fit is made for only two subshells: one for Ni-Ni and one for Ni-Mo, the weighting of these subshells being determined from the XRD results. Thus, using this combination of techniques, the number of independent parameters is considerably reduced.

## IV. RESULTS AND DISCUSSION

### A. Long-range order versus milling time

Figure 3 shows the XRD patterns of the Mo<sub>50</sub>Ni<sub>50</sub> system subjected to MA at increasing times. Initially (lower curve) the spectrum consists of a weighted sum of the powder patterns of bcc Mo and fcc Ni. From a deeper inspection in the pattern of untreated sample, the line profiles appear slightly broader than the instrumental resolution due to a weak combination of size and/or strain effects which are present in the as-received commercial powders.

A mechanical process of 2 h is already sufficient to induce a considerable broadening in the diffraction line profiles, reflecting the likely presence of particle-size reduction and increased lattice disorder. The effect is more marked after 5-h milling time although an additional feature is worthy of note; the Ni fcc (111) and (200) peak profiles are considerably asymmetric and the (220), (311), and (222) lines are partially overlapped with the nearby Mo profiles. At this stage of milling the pattern can still be decomposed into just the Ni (fcc) and Mo (bcc) components which, although highly distorted, represents a crystalline phase.

After milling the powder for 10 h the fcc Ni line profiles are completely absent in the pattern and an amor-

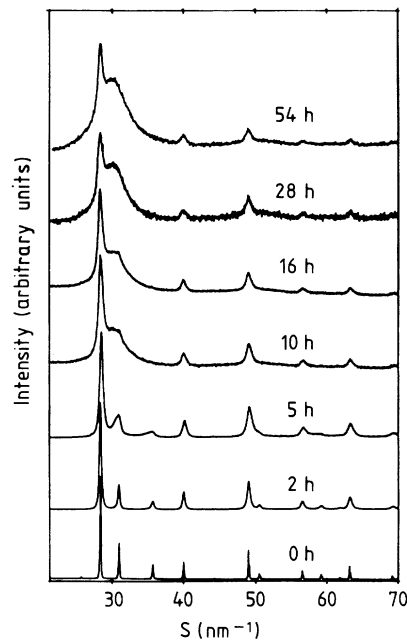


FIG. 3. X-ray powder diffraction data taken of NiMo as a function of milling time showing the formation of an amorphous phase after  $\approx 10$  h.

phous NiMo phase as demonstrated by the well-defined bump at  $\approx 30$  nm<sup>-1</sup> is observed together with the broadened peak profiles of the bcc Mo metallic phase. These persist with further broadening in the pattern even after milling for 16 and 28 h and are accompanied by an increase in the amorphous contribution to the total pattern. The lattice parameter of bcc Mo calculated from the position of the observable line profiles remains unchanged during the milling. The latter is expected given the nonsolubility of Ni in Mo reported in the phase diagram,<sup>24</sup> where, in contrast, Mo is reported soluble in Ni up to 20 wt. % at room temperature.

Figure 4 shows an enlarged view of the zone in the XRD data which encompasses the (110) Mo bcc and the (111) Ni fcc line profiles, together with the first halo associated with the amorphous phase. For the samples milled up to 10 h there is some merit in including in the fit a profile which corresponds to the (111) Ni line. The wave-vector location of this line gives a lattice parameter of 0.351 nm which is close to the crystallographic value of 0.3524 nm for pure Ni. However, for the samples milled for 28 h and longer no trace of this peak is observed. Table II shows the estimated composition of the amorphous phase as deduced from the ratio of the area encompassed by the (110) Mo bcc line profile to that under the amorphous halo as a function of milling time. In this case, the crystallinity,<sup>12</sup> i.e., the fraction of crystalline substance in the sample, clearly refers to the Mo bcc phase. From these we are able to calculate the amorphous phase which, after some 54 h of milling, results in a nominal composition of Ni<sub>50</sub>Mo<sub>38</sub>. Both the shape and position of this main halo for the amorphous phase does not significantly change with the milling time. If we apply the Ehrenfest relation<sup>25,26</sup> for the position of the main

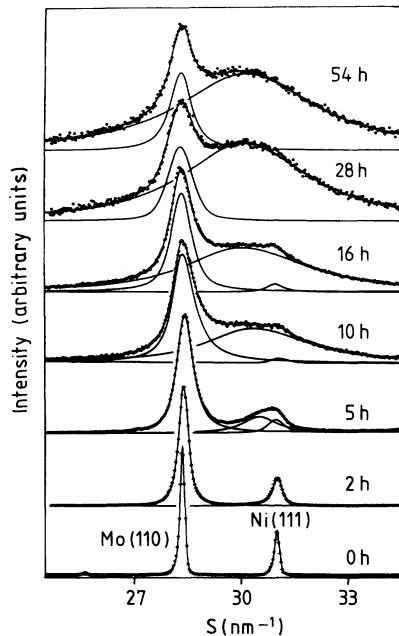


FIG. 4. Selected area of Fig. 1 showing in detail the x-ray line profiles for Mo(110) and Ni(111). Curve deconvolution shows the loss of the Ni(111) peak at  $\approx 10$  h milling time and the development of the NiMo amorphous phase. The bcc Mo(110) remains but is considerably broadened with milling time due to increased lattice strain.

halo, we obtain a nearest-neighbor distance of 0.256 nm, a value which is shorter than the average of Ni-Ni and Mo-Mo distances in pure metals. As the Ehrenfest equation was worked out for diatomic gaseous molecules this result should be used with some caution.

Although it is generally maintained that a large negative heat of mixing is a necessary condition to establishing amorphization, recently Gaffet and Harmelin<sup>27,28</sup> have reported partial amorphization by ball milling pure silicon and germanium powders. To determine whether a similar process was taking place in NiMo we have examined a pure fcc Ni powder which had been milled for 16 h. The results are given in Fig. 5 together with the patterns of unmilled and of 16-h MA Ni<sub>50</sub>Mo<sub>50</sub>, in the wave-vector range where the first amorphous halo of the NiMo alloy is expected. For the pure Ni powder a perfectly linear background can be traced under the (111) and (200) peaks after carrying out our numerical procedure. This means that under MA the pure Ni, al-

TABLE II. Estimated amorphous alloy composition calculated using Eq. (4) based on the ratios of the measured areas of the Mo(110) peak profile to the amorphous halo centered at a scattering wave vector around  $30 \text{ nm}^{-1}$  in Fig. 3.

Milling time (h)	Ratio of $I_{\text{Mo(110)}}/I_{\text{amor}}$	Amorphous alloy composition
10	0.48	Ni <sub>50</sub> Mo <sub>17</sub>
16	0.38	Ni <sub>50</sub> Mo <sub>22</sub>
28	0.24	Ni <sub>50</sub> Mo <sub>31</sub>
54	0.14	Ni <sub>50</sub> Mo <sub>38</sub>

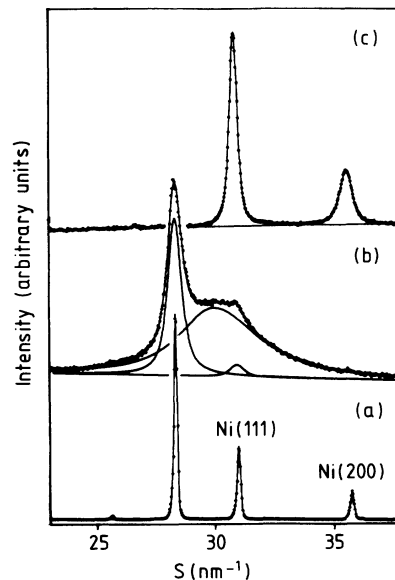


FIG. 5. X-ray powder patterns comparing the milling of NiMo with that of pure Ni powder illustrating that *a*-Ni is not formed on milling the pure metal. (a) NiMo after no milling, (b) NiMo milled for 16 h, and (c) pure Ni milled for 16 h.

though fragmented and distorted, maintains the original fcc structure and no transformation to a pure Ni amorphous phase is observable. This contrasts the behavior of the Ni<sub>50</sub>Mo<sub>50</sub> milled for the same time and points out the importance of a small negative excess of enthalpy of mixing.

Further structural information comes from the analysis carried out, using the simplified method, on the line profiles of the Mo XRD peaks. Figure 6 shows the integral breadth ( $\Delta S$ ) plotted as a function of the square of the profile  $S_{hkl}$  position. In the unmilled samples the broadening is distributed uniformly in reciprocal space which suggests an absence of any significant distortion in the "as-received" metallic powders. Conversely a marked slope, due to strain, can be seen in the data for the samples milled for 2 h. This further increases to

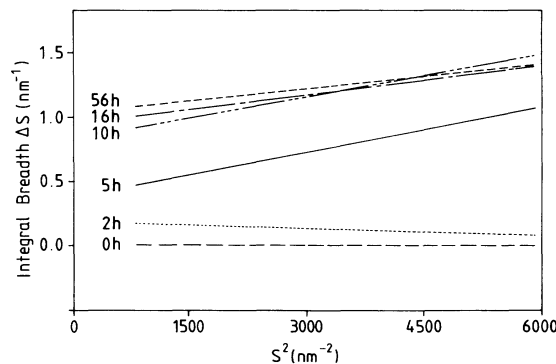


FIG. 6. Plot of the integral breadth against the square of the scattering vector for the Mo peak profiles for the (110), (200), (211), (220), (310) and (321) reflections measured as a function of milling time. The slopes of these linear plots are proportional to the strain disorder induced by the milling process whilst the intercept is proportional to the particle size.

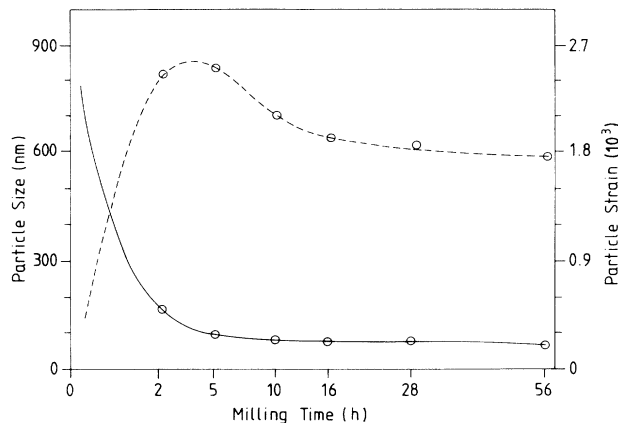


FIG. 7. Results of the Warren Averbach analysis of the data given in Fig. 3 showing the crystallite strain (a) and particle size (b) as a function of milling time. The data is deduced using the (110) and (220) reflections.

$\approx 2.5 \times 10^{-3}$  in the 5-h milled sample but decreases slightly before leveling off at  $\approx 1.8 \times 10^{-3}$  somewhere between the 50 and 10-h milling time from where it remains constant up to milling times of 54 h. These results are mirrored in the more detailed WA Fourier analysis summarized in Fig. 7. The coincidence of the two analyses confirm the lack of any significant preferred orientation effects during milling. The increase in particle strain is closely paralleled by the decrease in particle size down to constant value of  $\approx 70$  nm at 5–10 h of milling. The leveling off of both particle size and strain effects as evidenced from Figs. 6 and 7 directly correlates with the loss of crystalline order in the Ni fcc structure and the formation of an amorphous NiMo phase.

The decrease in the Mo particle size as function of MA treatment is in general agreement with observations on other systems such as NiTi (Ref. 29) and the overall strain behavior is interesting in that it reaches a maximum between 2 and 5 h MA before decreasing slightly. The exact mechanism associated with this strain relaxation is unclear but we note that the relaxation relates to the release of Mo into the amorphous alloy (see Table III) both from its bcc environment but more importantly from the distorted fcc phase formed between 2 and 5 h MA. We presume the loss of the latter defective structure is the essential precursor to the amorphous phase formation as evidenced after 10 h MA. Thermodynamically the NiMo (fcc) defective phase can be regarded as being a metastable precursor to the stable amorphous-phase formation which is energetically preferred as it releases the strain energy accumulated in the early (crys-

TABLE III. Least-squares fits to the Ni *K*-edge EXAFS data for the milling times up to 5 h.

Time	Atom	<i>N</i>	<i>r</i> (nm)	$\sigma^2$ (nm <sup>2</sup> )
0	Ni	12	0.249	0.000 10
2	Ni	8.6	0.249	0.000 11
	Mo	2.6	0.252	0.000 14
5	Ni	7.0	0.251	0.000 12
	Mo	3.2	0.255	0.000 13

talline) stages associated with the amorphous-phase formation by MA.

### B. Short-range order versus milling time

Ni and Mo *K* edge EXAFS data as a function of milling time are given in Figs. 8 and 9, respectively. The Ni data show that the Ni reference powder is clearly fcc; the first four shells are easily distinguishable. Up until 5 h

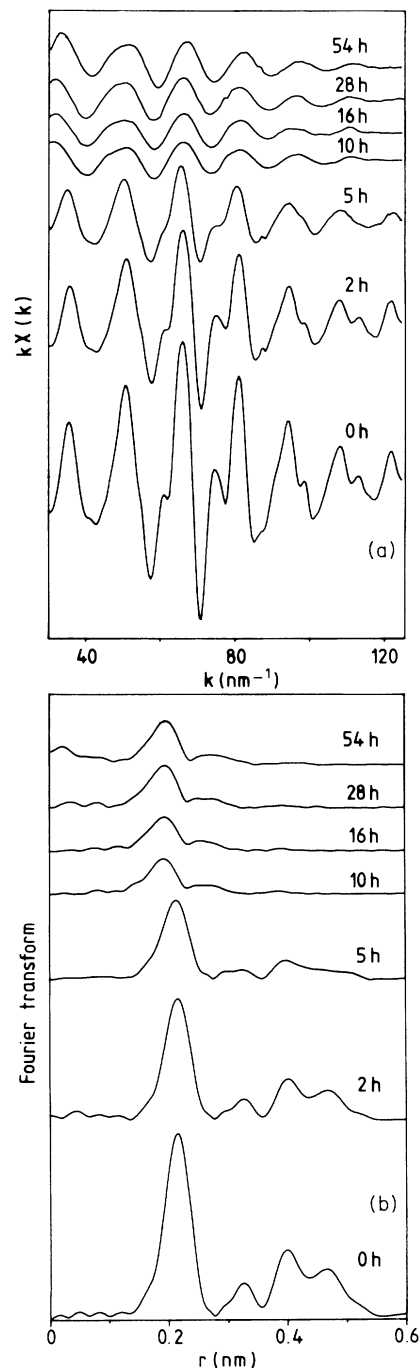


FIG. 8. Ni *K*-edge EXAFS data of NiMo as a function of milling time. Note the decrease in amplitude in the *k*-weighted EXAFS data (a) and the corresponding loss of long-range correlations in the corresponding Fourier transform (b) as a function of milling time.

there is a steady decrease in the EXAFS amplitudes and a change in the fine structure. This is mirrored by the changes in the Fourier transforms. The first shell is greatly reduced in amplitude and the more distant shells are strongly attenuated with respect to the first peak. For longer milling times (10 h and more) there are no more significant distant correlations and all the evaluable order is concentrated in the first shell. This evolves with mil-

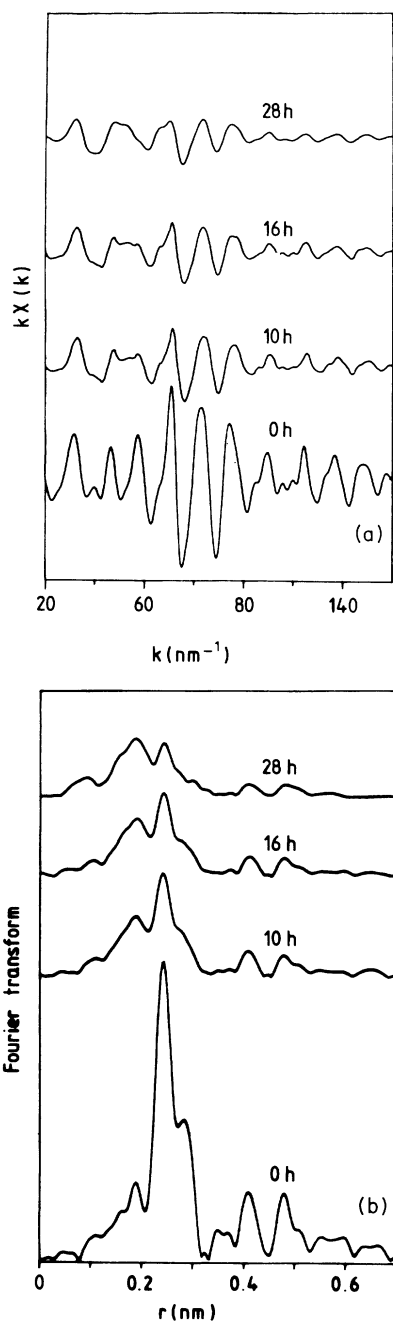


FIG. 9. Mo  $K$ -edge EXAFS data of NiMo as a function of milling time. Note that whilst there is a decrease in amplitude in the  $k$ -weighted EXAFS data (a) some long-range correlations can still be observed in the corresponding Fourier transform (b) as a function of milling time.

ling time, although the amplitude remains constant. The data taken at the Mo  $K$  edge show less dramatic changes as for all of the milling times used the bcc structure of bulk Mo is evident. It is clear, however, that the first-shell amplitude decreases with milling time, indicating a loss of Mo from the bcc structure and its presumed participation in the amorphization process.

For the reasons outlined in Sec. III B 3 a detailed analysis was only carried out on the Ni  $K$  edge data. Table III summarizes the modeled fits to the data taken at the intermediate milling times (2 and 5 h) and confirms the general trends found in the Fourier transforms, i.e., a gradual insertion of Mo into the Ni fcc lattice together with the associated dilation of the Ni-Ni and Ni-Mo correlations as function of milling time. For milling times greater than 5 h the use of such fitting to structurally characterize the amorphous phase is not realistic as the distance range of the Ni-Ni and Ni-Mo correlations becomes too broad to be modeled using two shells.

However, to highlight the effects of the antiphase cancellation effect we have fitted the 5-h spectrum to a single shell of Ni atoms at 0.249 nm. The coordination number is varied between 4 and 12 and by varying the correlation between  $N$  and  $\sigma$  the best fit was obtained. The results are summarized in Fig. 10 and clearly show that the best fit, without considering the effects of the phase of the Mo contributions is 6, is clearly unrealistic. In contrast a mixed Ni/Mo first shell provides a more realistic first shell of  $\approx 10$ –12 atoms. To confirm that this is relevant to our case we have plotted the difference in the phase function  $[\Delta(k)$ , see Eq. (9)] for Ni and Mo over the  $k$  range used in the EXAFS analysis for different values of  $r$  in Fig. 11. It shows that for small values of  $r$ , i.e., small differences between the Ni-Ni and Ni-Mo distances, the phases essentially cancel  $[\Delta(k) \approx \pi]$ , and thus, particularly for wave vectors greater  $\approx 60 \text{ nm}^{-1}$ , there will be a severe attenuation of  $\Delta(k)$ .

The validity of the mixed shell fit is further demonstrated in Fig. 12 which shows the correlation maps between the two subshell coordination numbers, i.e., Ni-Ni ( $N_1$ ) and Ni-Mo ( $N_2$ ) from the least-square fits to the spectra taken after 2- and 5-h milling. The importance of

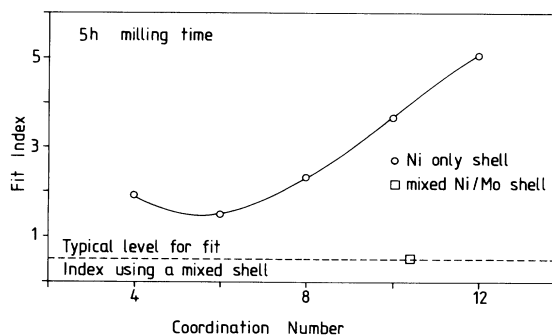


FIG. 10. Plot of the fit index as a function of coordination number for the 5-h milled sample, assuming only Ni atoms are present, demonstrating the effects of phase cancellation from the Mo backscattering atoms. The fit using the subshell analysis is also shown.

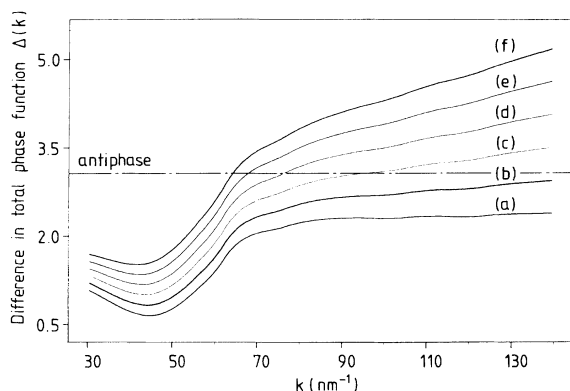


FIG. 11. Wave-vector-dependent total phase function  $[\Delta(k)]$  based on calculations of the backscattering amplitudes for different values of the difference  $(\Delta r)$  between Ni-Ni and Ni-Mo distances calculated from the data of Teo and Lee.<sup>20</sup>  $r$  (nm) = 0.0 (a), 0.02 (b), 0.04 (c), 0.06 (d), 0.08 (e), and 0.10 (f). The position for total phase cancellation  $[\Delta(k) = \pi]$  is marked.

using the correct phase shifts and accurate distances to determine the Ni-Ni and Ni-Mo correlations is clear. The same spectra could have been fitted equally well with one pure Ni shell with coordination numbers of  $\approx 6$  and  $\approx 4$ , respectively, which would not be a credible physical model for a metallic solid.

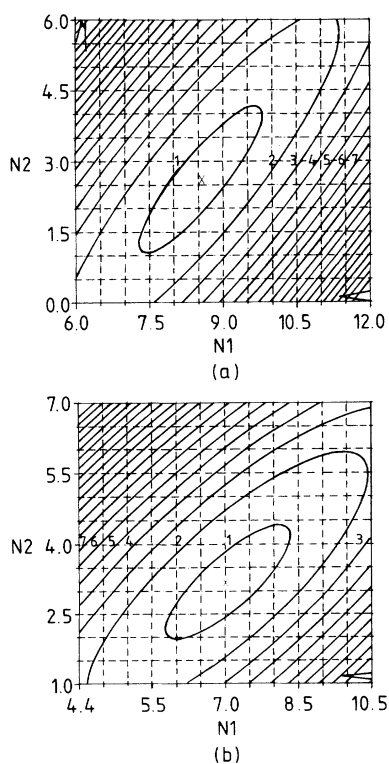


FIG. 12. Correlation plots produced from the MAP routine in EXCURVE88 for (a) milling time 2 h, contour increment 2.899, fit index 2.245, (b) milling time 5 h, contour increment 3.252, fit index 0.525, showing the correlation between the coordination numbers for Ni-Ni ( $N_1$ ) and Ni-Mo ( $N_2$ ) correlations.

The evolution of Ni-Ni and Ni-Mo correlations as a function of the amorphization process can be easily seen from the subshell analysis of the Fourier filtered Ni  $K$ -edge first-shell EXAFS data. The least-squares fits to these are shown in Fig. 13 together with the partial RDF's in the form of Gaussian-broadened histograms detailing the relative weighting of the Ni-Ni and Ni-Mo correlations which are shown in Fig. 14. For comparison Fig. 15 shows the corresponding broadened histogram for  $\delta$ -NiMo in comparison to the 54-h milled NiMo sample. It can be seen that after about 10 h milling time the Ni-Ni and Ni-Mo correlations remain fairly constant in mean distance but change in relative weighting as a function of milling. At 10 h the Ni-Ni distance dominates the intermetallic correlations as the amorphization process is in its early stage but the situation reverses by 54 h milling time which closely resembles the pair correlation expected for the amorphous  $\delta$ -NiMo. The 54-h milled NiMo differs from the latter in that the Ni-Ni correlations are broader than the pure alloy which in turn gives rise to the asymmetric peak profile of the partial RDF. This result is very similar to the amorphization reaction in a Zr-Co multilayered structure reported by Schroder, Samwer, and Koster.<sup>30</sup> In the solid-state amorphization reaction

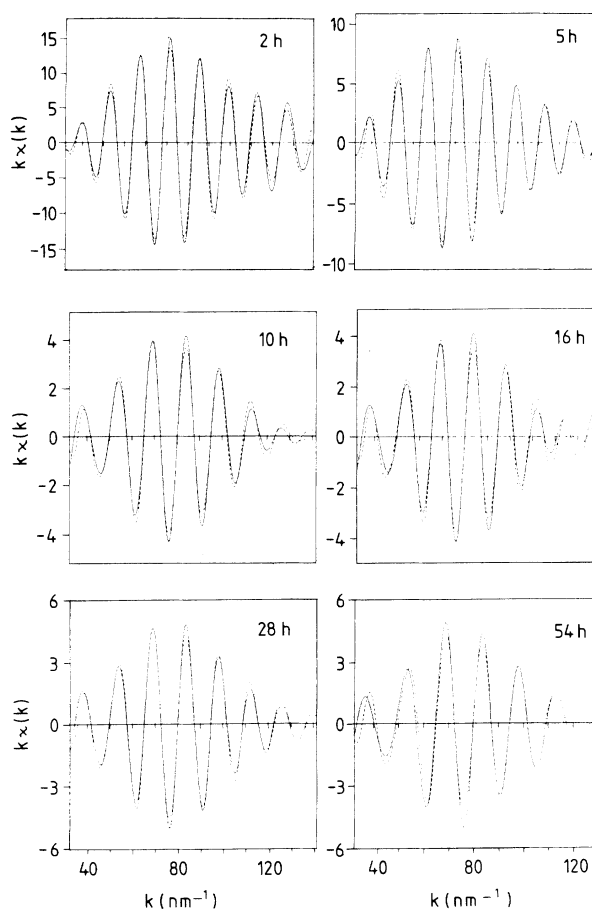


FIG. 13. Least-squares fits (---) to the Fourier filtered first-shell  $\chi(k)$  EXAFS data (—) as a function of milling time.

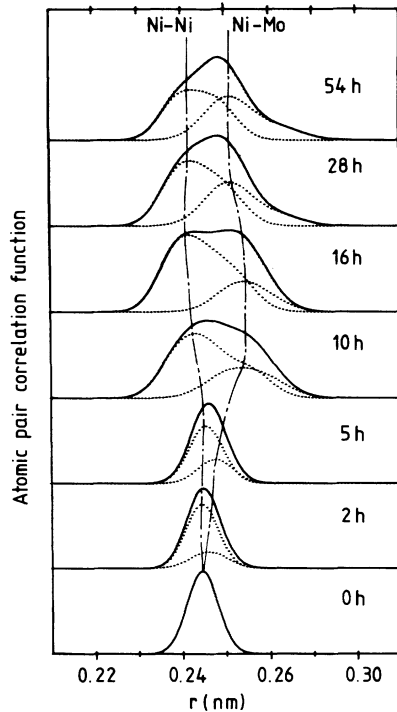


FIG. 14. Results of a subshell analysis of the Fourier-filtered first-shell Ni  $K$ -edge data displayed as a series of Gaussian-broadened histograms as a function of milling time.

(SSAR) studied by these authors, they found that initially cobalt was consumed and amorphous  $Zr_{20}Co_{80}$  was formed, and later the rest of the zirconium was consumed so that the final composition of the amorphous alloy became  $Zr_{40}Co_{60}$ . This shows once more the similarities between SSAR in thin multilayers and ball milling.<sup>12</sup>

## V. CONCLUSIONS

From this investigation it is clear that important structural changes occur around Ni and Mo during milling and that it is only with a combination of XRD and EXAFS analysis that we have been able to describe the kinetics of the reaction, the start of the amorphization, and the resulting solid structures. X-ray diffraction demonstrates that the cold work by MA introduces considerable strain both on the Ni and Mo phases. This observation is quantified through a comparison of the profile analysis (Fig. 7) and the subshell analysis of the Ni

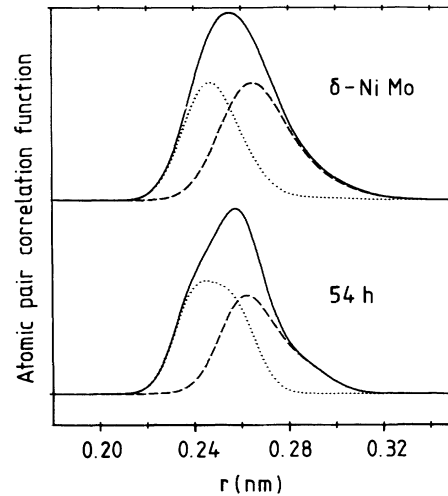


FIG. 15. Comparison of the 54-h milled sample from Fig. 13 with the corresponding histogram derived for  $\delta$ -NiMo.

$K$ -edge EXAFS data (Fig. 14) which show that the amorphous phase of NiMo nucleates after a substantial insertion of Mo into the fcc Ni lattice, until a critical internal stress is reached, followed by loss of long-range order. At the early stage of milling (2 h) some Mo diffuses into the Ni lattice taking advantage of the fragmentation of crystallites. This disorder increases at 5 h of milling with the Ni phase in a highly disordered condition when additional Mo was diffused into Ni. It is presumably in this condition of atomic concentration, disorder content, and size fragmentation that further MA drives a transformation to the amorphous condition, as actually manifested in the 10-h milled powder. The subsequent slow reactivity of the rest of the Mo towards an entirely amorphous condition can be explained by different solid solubilities of Mo in the  $Ni_xMo_{(1-x)}$  amorphous phase and in the fcc  $Ni_xMo_{(1-x)}$  phase.

## ACKNOWLEDGMENTS

This research has been carried out as part of the UK's Science and Engineering Research Council's specially promoted program in particulate technology. We gratefully acknowledge Daresbury Laboratory for the provision of beam time on the SRS.

<sup>1</sup>J. S. Benjamin and T. E. Volin, *Metall. Trans.* **5**, 1929 (1974).

<sup>2</sup>J. S. Benjamin, *Sci. Am.* **234**, 40 (1976).

<sup>3</sup>C. C. Koch, O. B. Cavin, C. G. McKamey, and J. O. Scarborough, *Appl. Phys. Lett.* **43**, 1017 (1983).

<sup>4</sup>Proceedings of the Conference on Solid State Amorphizing Transformations, Los Alamos, New Mexico, 1987 [*J. Less-Common Met.* **140** (1988)].

<sup>5</sup>A. E. Ermakov, E. E. Yivichikov, and V. A. Barinov, *Fiz. Met. Metallorod.* **52**, 1184 (1981).

<sup>6</sup>G. Cocco, I. Soletta, L. Battezzati, M. Baricco, and S. Enzo, *Philos. Mag.* **B 61**, 473 (1990).

<sup>7</sup>J. M. Dubois, *J. Less-Common Met.* **145**, 309 (1989).

<sup>8</sup>L. Battezzati, S. Enzo, L. Schiffrini, and G. Cocco, *J. Less-Common Met.* **145**, 301 (1988).

<sup>9</sup>G. N. Greaves, G. P. Diakun, P. D. Quinn, M. Hart, and P. Siddons, *Nucl. Instrum. Methods* **208**, 335 (1983).

<sup>10</sup>S. Enzo, A. Benedetti, and S. Polizzi, *Z. Kristallogr.* **170**, 275 (1985).

- <sup>11</sup>S. Enzo, G. Fagherazzi, A. Benedetti, and S. Polizzi, *J. Appl. Crystallogr.* **21**, 536 (1988).
- <sup>12</sup>G. Cocco, S. Enzo, L. Schiffini, and L. Battezzati, *Mater. Sci. Eng.* **97**, 43 (1988).
- <sup>13</sup>H. P. Klug and L. E. Alexander, *X-ray Diffraction Procedures* (Wiley, New York, 1974), p. 634.
- <sup>14</sup>B. E. Warren and B. L. Averbach, *J. Appl. Phys.* **21**, 595 (1950).
- <sup>15</sup>B. H. Williamson and W. H. Hall, *Acta Metall.* **1**, 22 (1953).
- <sup>16</sup>S. J. Gurman, *J. Phys. C* **21**, 3699 (1988).
- <sup>17</sup>B. K. Teo, H. S. Chan, R. Wang, and M. R. Antonio, *J. Non-Cryst. Solids* **58**, 249 (1983).
- <sup>18</sup>E. Pantos and G. D. Firth, in *EXAFS and Near Edge Structure III*, edited by K. O. Hodgson, B. Hedman, and J. E. Penner-Hahn (Springer-Verlag, Berlin, 1984), p. 110.
- <sup>19</sup>S. J. Gurman, *J. Mater. Sci.* **14**, 1541 (1982).
- <sup>20</sup>B. K. Teo and P. A. Lee, *J. Am. Chem. Soc.* **101**, 2815 (1979).
- <sup>21</sup>M.R. Antonio, B. K. Teo, W. E. Cleland, and B. A. Anevill, *J. Am. Chem. Soc.* **105**, 3477 (1983).
- <sup>22</sup>C. B. Shoremaker and D. P. Shoemaker, *Acta Crystallogr.* **16**, 997 (1963).
- <sup>23</sup>G. N. Greaves, N. T. Barrett, G. M. Antonini, F. R. Thornley, B. T. M. Willis, and A. Steel, *J. Am. Chem. Soc.* **111**, 4313 (1989).
- <sup>24</sup>M. Hansen, *Constitution of Binary Alloys* (McGraw-Hill, New York, 1985), p. 968.
- <sup>25</sup>P. Ehrenfest, *Proc. Amst. Acad.* **17**, 1132 (1919).
- <sup>26</sup>A. Guinier, *X-ray Diffraction* (Freeman, San Francisco, 1963), p. 73.
- <sup>27</sup>E. Gaffet and M. Haramel, *J. Less-Common Met.* **157**, 201 (1990).
- <sup>28</sup>E. Gaffet, *J. Less-Common Met.* (to be published).
- <sup>29</sup>R. Schultz, M. Trudeau, J. Y. Haet, and A. van Neste, *Phys. Rev. Lett.* **62**, 2849 (1989).
- <sup>30</sup>H. Schroder, K. Samwer, and U. Koster, *Phys. Rev. Lett.* **54**, 197 (1985).